JGR Space Physics

RESEARCH ARTICLE
10.1029/2024JA032864

The Morphology and Oscillations of Nightside Mid-Latitude Ionospheric Trough at Designated Longitudes in the Northern Hemisphere

Xinlong Liu[1], Donghe Zhang[1], Anthea J. Coster[2], Zhonghua Xu[3], Xueling Shi[3,4], and Shibaji Chakraborty[3]

[1]School of Earth and Space Science, Peking University, Beijing, China, [2]Haystack Observatory, Massachusetts Institute of Technology, Millstone Hill, MA, USA, [3]Center for Space Science and Engineering Research, Virginia Tech, Blacksburg, VA, USA, [4]High Altitude Observatory, National Center for Atmospheric Research, Boulder, CO, USA

Key Points:

- The minimum position of mid-latitude ionospheric trough shows discernible longitudinal variation
- Three distinct periodic components were observed in the trough's minimum position: 27, 13.5, and 9 days
- High latitude ionospheric plasma convection plays an important role in controlling the trough's minimum position

Correspondence to:
D. Zhang,
zhangdh@pku.edu.cn

Citation:
Liu, X., Zhang, D., Coster, A. J., Xu, Z., Shi, X., & Chakraborty, S. (2024). The morphology and oscillations of nightside mid-latitude ionospheric trough at designated longitudes in the Northern Hemisphere. *Journal of Geophysical Research: Space Physics*, *129*, e2024JA032864. https://doi.org/10.1029/2024JA032864

Received 8 MAY 2024
Accepted 12 SEP 2024

Abstract The mid-latitude ionospheric trough (MLIT), an anomaly in the ionosphere's F layer caused by various mechanisms, affects radio wave propagation. In this study, we investigated the morphology and oscillations of the MLIT using global Global Positioning System total electron content map data between 1 January 2018, and 31 December 2020. The MLIT position varies longitudinally, reaching its farthest equatorward at 60°W and its farthest poleward at 30°E. The MLIT occurrence rates peak during the winter and equinoxes and dip in summer, while seasonal variations in MLIT position vary across longitude bands. Heightened geomagnetic activities, quantified by the SME6 index, promote MLIT occurrence, especially during pre-midnight hours in summer and equinoxes, and shift the MLIT equatorward, particularly during midnight and post-midnight hours. The MLIT position shows clear local time variation, with a gradual decrease before midnight, stabilization afterward, and a minor resurgence around dawn. Wavelet analysis reveals three distinct periodic components in the MLIT position: 27, 13.5, and 9, with the 27-day period being the most persistent. Cross-wavelet and wavelet coherence analyses suggest that solar wind (SW) velocity variations precede changes in the MLIT position. The main factors responsible for the equatorward movement of MLIT are the electric fields in high-speed SW that enhance the ionospheric convection pattern, and the intensified geomagnetic activities induced by interplanetary shocks.

1. Introduction

The mid-latitude ionospheric trough (MLIT) is one of the main latitudinal structures of ionosphere, which was first discovered by Muldrew (1965) and Sharp (1966). The MLIT, a plasma density attenuation structure in the F layer, mainly occurs in the narrow boundary region between the mid-latitudes and the auroral zone (Moffett & Quegan, 1983; Rodger et al., 1992; Scali, 1992). The emergence of MLIT results in significant electron density gradients in the F layer, consequently influencing the propagation of radio waves.

Various physical mechanisms contribute to the MLIT's formation, with the dominant one varying based on geomagnetic conditions (Rodger, 2008; Rodger et al., 1992). These mechanisms mainly include stagnation mechanism, enhanced recombination processes, and precipitation and transport. The stagnation mechanism occurs when opposing convective and co-rotating electric fields significantly reduce plasma velocity in the mid-latitudes (Collis & Häggström, 1988; Rodger et al., 1992; Spiro et al., 1978; Whalen, 1989), allowing the plasma to recombine over a longer period, and consequently decreasing plasma density at night. The enhanced recombination processes are primarily due to the increased recombination rate of oxygen ions (O^+) caused by a rise in ion temperature (Rodger, 2008; Rodger et al., 1992; Schunk et al., 1976). This temperature rise can result from frictional heating between ions and neutral particles during subauroral ion drifts (SAID) (Spiro et al., 1979). Additionally, frictional heating in the E layer may lead to a higher average molecular weight (Rishbeth et al., 1985), further enhancing the recombination processes. The MLIT's poleward boundary is shaped by precipitated auroral particles (Rodger et al., 1986), while its equatorward boundary is formed by downward oxygen ions from the nightside plasmasphere (Yizengaw et al., 2005) and photoionized plasma transported from the dayside due to the Earth's rotation (Voiculescu et al., 2010). In general, the MLIT's formation is a complex process involving numerous physical mechanisms. Rodger et al. (1992) detailed the relative importance of each mechanism under different geomagnetic conditions.

The morphology of the MLIT, or its position and shape, is generally described by three parameters: the equatorward boundary, the minimum position, and the poleward boundary. For the sake of simplicity, the term "MLIT position" will be used hereafter to refer specifically to the MLIT's minimum position. Some researchers defined more parameters to describe the MLIT's fine structure, for example, the breakpoints and the trough width (Pryse et al., 2006), the trough depth, the equatorward and the poleward half-width (Yang et al., 2015). All these parameters are affected by season, longitude, local time (LT), geomagnetic activity and solar activity. A multitude of studies indicated that the MLIT predominantly occurs on the nightside over a broad LT range, with its presence being especially prominent during the winter and equinoctial seasons. However, during the summer, the MLIT's occurrence is primarily concentrated in the post-midnight sector and is less distinct compared to other seasons (M. S. He et al., 2011; Ishida et al., 2014; Lee et al., 2011; Matyjasiak et al., 2016; Rodger et al., 1992; Voiculescu et al., 2006). Tulunay (1973) first identified the longitudinal variation of the MLIT, and Horvath and Essex (2003) attributed it to influences such as geomagnetic field strength, geomagnetic declination, and the solar position with respect to the magnetic equator using the total electron content (TEC) data acquired from the TOPEX satellite. Besides, the MLIT's morphology varies with changes in LT (Collis & Häggström, 1988; Karpachev, 2003; Karpachev et al., 1996; Lee et al., 2011; Parker et al., 2018; Spiro et al., 1978). The influence of geomagnetic activity on the MLIT's morphology has been extensively studied using various geomagnetic indices, with a consensus on the inverse linear correlation between the MLIT position latitude and the Kp index (Collis & Häggström, 1988; Krankowski et al., 2009). Werner and Prölss (1997) considered the "memory effect," suggesting that the MLIT position is influenced not only by current geomagnetic activities but also by past activities. Consequently, they introduced the AE6 index by integrating the Auroral Electrojet (AE) index from the prior 6 hr into the current AE index, with Prölss (2007) noting its superior correlation with the MLIT position compared to traditional indices like Kp, AE, and Dst. Following the concept of the AE6 index, S. C. He et al. (2020) introduced the Kp9 index, demonstrating that its correlation with the MLIT position is stronger than that of the AE6 index. In addition to the MLIT position, Karpachev (2003) also indicated that when the Kp index increases from 2 to 5, the MLIT generally becomes broader and deeper, which is associated with the influence of disturbed electric fields. Moreover, solar activity has been observed to influence the MLIT's morphology. Ishida et al. (2014) noted that the MLIT deepens as the F10.7 index rises using data from the European Incoherent Scatter Radar, which is primarily due to enhanced recombination processes. Employing Global Positioning System (GPS) TEC map data, Le et al. (2017) discovered that under quiet geomagnetic conditions (Kp < 3), the magnetic latitude (MLAT) of MLIT position decreases from 60° to 58° as the F10.7 index rises from 70 to 170 solar flux units (sfu). Using GNSS (Global Navigation Satellite System) TEC data, Castaño et al. (2021) found that from low to high solar activity, the MLATs of MLIT position in the Northern and Southern Hemispheres shift toward the equator by approximately 3° and 1°, respectively.

In recent years, research has increasingly shown a close relationship between the oscillations in the MLIT position and variations in specific parameters of the solar wind (SW) (Castaño et al., 2021; M. S. He et al., 2011; Natali et al., 2020). Using electron density data from the COSMIC satellites, M. S. He et al. (2011) revealed the first observations of a 9-day periodic oscillation in the MLAT of MLIT position, which has an amplitude of approximately 1° to 1.5° and is closely aligned with high-speed SW appearing on a 9-day cycle. Additionally, they discovered a longitudinal dependence that the deepest MLIT at midnight occurs within the 150°W to 90°W sector in the Northern Hemisphere, west of the northern geomagnetic pole. Natali et al. (2020) utilized GPS TEC map data to discern oscillation periods of 9 and 27 days in the MLIT position at 00 LT and 02 LT during solar minimum, which exhibit a robust association with oscillations in SW velocity. They suggested that the SW velocity and the interplanetary magnetic field (IMF) could jointly influence high-latitude ionospheric plasma convection driven by local electric fields, expressible by the equation $\boldsymbol{E}_{SW} = -\boldsymbol{V}_{SW} \times \boldsymbol{B}_z$ in the Earth's frame (Burton et al., 1975), thereby directly affecting the MLIT position. Castaño et al. (2021) observed 13.5-day and 27-day periodicities in the MLIT position in both hemispheres using GNSS TEC map data. They found that these periodicities are most evident in the spring and autumn during the descending and minimum phases of the solar cycle, which can be attributed to the impact of SW velocity and IMF B_z component on high-latitude ionospheric plasma convection. However, they assumed that the ionization only depends on LT and globally averaged the TEC latitude profiles corresponding to fixed LT, neglecting the effect of longitude. Beyond the 9-, 13.5-, and 27-day periodicities, SW velocity and geomagnetic indices were found to exhibit oscillation periods of less than 9 days during descending and minimum phases of the 23rd solar cycle (Gibson et al., 2009; Temmer et al., 2007). These periodic oscillations in the SW are induced by coronal holes that are distributed at certain intervals in solar

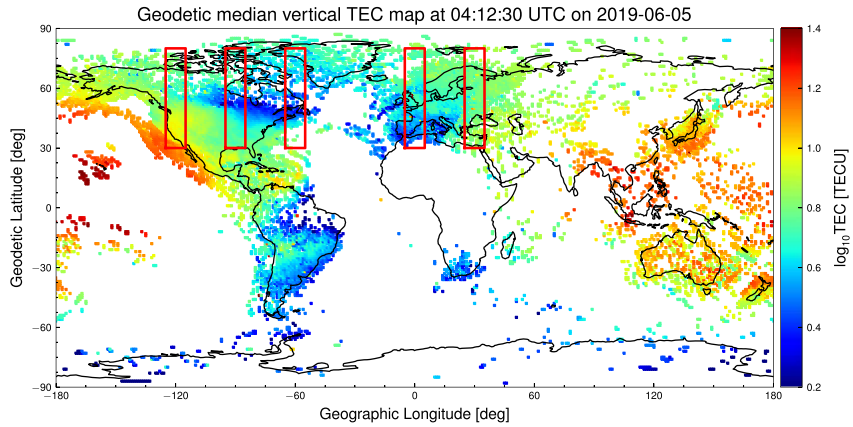

Figure 1. Global vertical total electron content (TEC) map at 04:12:30 UTC on 5 June 2019. This map presents the global coverage of the Global Positioning System TEC data with five 10-degree wide longitude bands marked by red rectangles, centered at 120°W, 90°W, 60°W, 0°, and 30°E.

longitude, reflecting the Sun's approximately 27-day rotation cycle. For example, the 9-day oscillation can be caused by three coronal holes that are spaced about 120° apart (Temmer et al., 2007). The coronal holes predominantly occur during the descending and minimum phases of the solar cycle. These regions allow for easier escape of high-energy particles into interplanetary space, hence serving as principal sources of high-speed SW streams (Emery et al., 2009; Krieger et al., 1973).

The morphological changes of the MLIT were extensively studied more than 10 years ago. However, with the increasing number of ground GPS receivers, there has been a continuous improvement in TEC data quality. Given these advancements, it becomes vital to reanalyze the MLIT's morphological changes using newer data. Moreover, the newly discovered association between oscillations in the MLIT position and variations in SW parameters could deepen our understanding of the underlying physical mechanisms behind MLIT. This study aims to advance our understanding of the MLIT's morphological changes and oscillations by analyzing GPS TEC map data from 2018 to 2020 in the Northern Hemisphere, considering longitudinal dependence. In the following Section 2, we introduce the data used in this study and the method of identifying the MLIT. Section 3 and Section 4 present the results and the discussion of our analysis, respectively. Finally, we summarize our main findings in Section 5.

2. Data and Methods

2.1. Data and Preprocessing

In this study, we used the global GPS TEC maps generated by the Massachusetts Institute of Technology (MIT) Haystack Observatory using the MAPGPS (MIT Automated Processing of GPS) software (Rideout & Coster, 2006; Vierinen et al., 2016). We downloaded these TEC maps in the CEDAR Madrigal Database. These maps feature a spatial resolution of $1° \times 1°$ and a temporal resolution of 5 min, extending from 1998 to the present. However, the spatial coverage of the maps is inherently limited by the distribution of ground GPS receivers. With the passage of time, there has been a progressive increase in the coverage of ground GPS receivers. Concurrently, the computational algorithms for processing GPS data have been undergoing continuous enhancement. To ensure accurate analysis, we used TEC maps from the recent solar minimum period (2018/1/1 to 2020/12/31). Figure 1 illustrates the global coverage of the GPS TEC data during this time, highlighting better coverage in America and Europe. Therefore, we chose five 10-degree-wide longitude bands in these areas, centered at 120°W, 90°W, 60°W, 0°, and 30°E. These longitude bands are marked by red rectangles in Figure 1. Subsequently, from available TEC maps, we extracted nightly latitude profiles across five longitude bands for each day. These profiles were then averaged every local hour, resulting in a data set of 65,760 individual TEC latitude profiles.

To investigate the effect of geomagnetic activity on the MLIT, we used the SuperMAG Electrojet (SME) index data obtained from the SuperMAG website. The SME index, which measures the strength of geomagnetic

disturbances from mid-latitudes to auroral zones, is calculated using data collected by over 100 ground-based magnetometers located in the Northern Hemisphere, covering MLATs from 40° to 80° (Newell & Gjerloev, 2011). Notably, this index offers superior temporal and spatial resolutions compared to the traditional AE index (Bergin et al., 2020). Given that the TEC latitude profiles have a 1-hr temporal resolution, we averaged the SME index over 1-hr periods. Furthermore, emulating the calculation approach of the AE6 index (Werner & Prölss, 1997), we integrated the SME index from the previous 6 hr into the current SME index to compute the SME6 index:

$$SME6 = \frac{\sum_{i=0}^{6} SME_{UT-i[h]} \cdot \mathrm{e}^{-i}}{\sum_{i=0}^{6} \mathrm{e}^{-i}}. \quad (1)$$

Subsequently, we classified SME6 < 200 nT as indicating low levels of geomagnetic activity, which accounted for 75.9% and SME6 ⩾ 200 nT as indicating high levels of geomagnetic activity, which accounted for 24.1% of the nighttime period over three years, between 2018 and 2020.

The SW and IMF data employed in this study were obtained from the OMNI data set hosted on the NASA Coordinated Data Analysis Web (CDAWeb). We utilized measurements including SW velocity, SW density, and the IMF B_z component to investigate the association between the MLIT position oscillations and SW variations. These data sets are primarily derived by temporally shifting observations from the ACE and Wind spacecraft, which are positioned near the L1 Lagrange point in the Sun-Earth system, to the Earth's bow shock nose.

The Super Dual Auroral Radar Network (SuperDARN) is a global network of high frequency ($3-30$ MHz) coherent scatter radars monitoring conditions in the near-Earth space environment (e.g., Chisham et al., 2007; Nishitani et al., 2019). The radars allow us to map the large-scale ionospheric convection patterns in the Northern and Southern Hemispheres with high temporal resolution (2 min, Ruohoniemi et al., 1989; Thomas & Shepherd, 2018). In this study, we used the SuperDARN data including the Cross Polar Cap Potential (CPCP) and the Heppner-Maynard Boundary (HMB) to investigate the association between the MLIT position oscillations and ionospheric convection patterns. Additionally, the number of velocity vectors (NVV) was used to evaluate the quality of the SuperDARN data. The NVV is defined as the total NVV measured by all radars, which is used for fitting to obtain the ionospheric convection patterns. To ensure data reliability, we retained only the CPCP and HMB entries with NVV values over 50.

2.2. Method of Identifying the MLIT

Due to the presence of some anomalous phenomena in the ionosphere, such as the equatorial ionization anomaly and high-latitude troughs, the identification of MLIT is often complicated. Besides, the accuracy of the identification of MLIT's structural parameters is not consistently high. Thus, we focused only on the MLIT's minimum position (MLIT position hereafter) in this study. We first adopted an automated algorithm to identify the MLIT position in the Northern Hemisphere, involving the following steps:

1. For a given TEC latitude profile, local minima between 45° and 70° magnetic latitudes are identified. These points serve as initial markers from which the search extends equidistantly toward both the northern and southern directions until a local maximum is encountered on either side, or until the latitudinal width exceeds 20°, delineating potential trough regions.
2. Trough regions with equatorward boundaries below 40° or poleward boundaries above 80° are excluded.
3. Trough regions where data coverage on one side of the minimum falls below 50% are discarded.
4. Trough regions that do not meet the criterion $TEC_{\min} < (1 - w/200)\, TEC_{mean}$ are removed, where w is the trough's latitudinal width and TEC_mean is the mean TEC value of the trough region.
5. If a single trough region remains, it is recognized to be the MLIT. Otherwise, the trough region closest to the equator is selected as the MLIT. In the absence of any qualifying trough regions, the existence of the MLIT is not recognized.

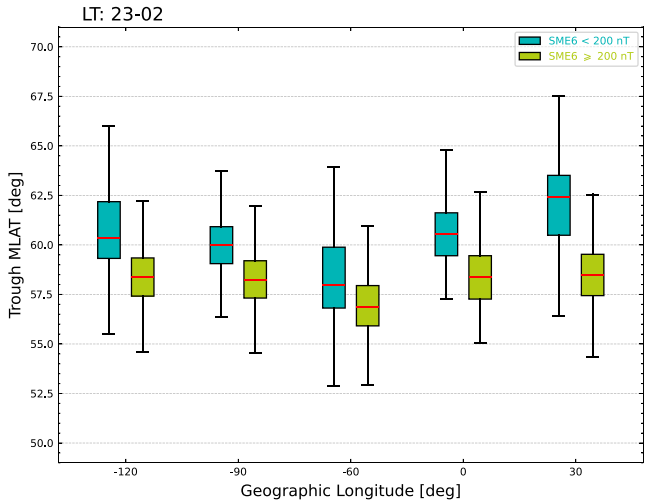

Figure 2. Variation of the mid-latitude ionospheric trough (MLIT) minimum position by longitudinal bands and geomagnetic activity. This figure illustrates the distributions of MLIT position in magnetic latitude across five longitudinal bands under two different geomagnetic activity levels, using box-and-whisker plots for visualization.

Utilizing the above algorithm, our automated program successfully identified 49,499 MLITs from all the TEC latitude profiles. After a thorough manual review, we eliminated 1,554 incorrectly recognized features, resulting in a refined data set of 47,975 MLITs.

3. Results and Analysis

3.1. Longitudinal Variation

In this study, we employed the Altitude Adjusted Corrected Geomagnetic (AACGM) (Shepherd, 2014) coordinates system to transform geographic latitudes into MLATs at an altitude of 350 km, facilitating an investigation into the distribution characteristics of the MLIT position under various conditions. First, we analyzed the longitudinal variation in MLIT position under different levels of geomagnetic activity, as illustrated by box-and-whisker plots in Figure 2. The analysis reveals that during periods of low geomagnetic disturbance (blue boxes), the MLATs of MLIT position across all longitude bands predominantly cluster around 58° ∼62°N. In contrast, under conditions of high geomagnetic disturbance (acid green boxes), a decrease in the MLATs of MLIT position across all longitude bands is observed, with an average reduction of approximately 2° as the SME6 index shifts from below 200–200 nT or above. The following sections will explore in detail the impact of geomagnetic activity on the MLIT position. Moreover, longitude-wise, the 60°W longitude band features the lowest MLATs of the MLIT position, whereas the 30°E longitude band records the highest MLATs, with the remaining three longitude bands showing only slight differences between them. Thus, the MLIT's longitudinal variations should not be ignored, which is also highlighted by Karpachev (2003). For subsequent analyses, we restrict our focus to the 120°W and 90°W longitude bands, chosen for their similar MLIT position distributions and geographical proximity. Additionally, a comparison of MLIT position distributions under different levels of geomagnetic activity suggests that not only does the MLATs of MLIT position decrease under high geomagnetic disturbances, but the longitudinal variation is also reduced.

3.2. Seasonal and LT Variations

Figure 3 presents the seasonal and LT variations in the MLIT occurrence rate. Due to the good temporal continuity of the TEC data, we directly present the monthly MLIT occurrence rate, defined as the ratio of MLIT instances to total TEC latitude profiles for specific local times. As can be seen, the MLIT occurrence rate is consistently at its nadir in the summer, a pattern significantly distinct from that observed in other seasons. Minimal differences are detected between the equinoxes and winter, with the peak incidence occurring during the pre-midnight hours in winter, and the post-midnight hours in the equinoxes. These results are similar to the findings shown by Ishida et al. (2014). Additionally, the diurnal amplitude of the seasonal variations is most subdued around midnight, whereas it is substantially larger during the pre-midnight and post-midnight hours. The data also confirm that geomagnetic activity significantly stimulates the genesis of the MLIT. This effect is most apparent before midnight in summer and least noticeable after midnight during the equinoxes.

Figure 4 depicts the MLIT position distributions for various months under different geomagnetic conditions during the midnight local times (23–02 LT), across different longitude bands. Notably, seasonal variations exhibit distinct patterns depending on the longitude band. The seasonal variations are most pronounced in the 0° and 30°E bands, with the MLIT position being most equatorward in summer and most poleward in equinoxes and winter. In contrast, the seasonal variations are not conspicuous in the 120°W, 90°W and 60°W bands. This suggests that the MLIT's seasonal variations are influenced by its longitudinal changes, similar to the findings reported by Matyjasiak et al. (2016). Combined with Figure 2, we can find that in the 0° and 30°E longitude bands with noticeable seasonal variations, the MLIT shifts away from the equator, while in the 120°W, 90°W and 60°W bands with weaker seasonal variations, the MLIT remains closer to the equator. Furthermore, under conditions of intense geomagnetic activity (illustrated in Figure 4 on the right), the seasonal variations tend to diminish, and the monthly distributions become more concentrated, as indicated by the reduced spacing between the upper and lower bounds of the box plots.

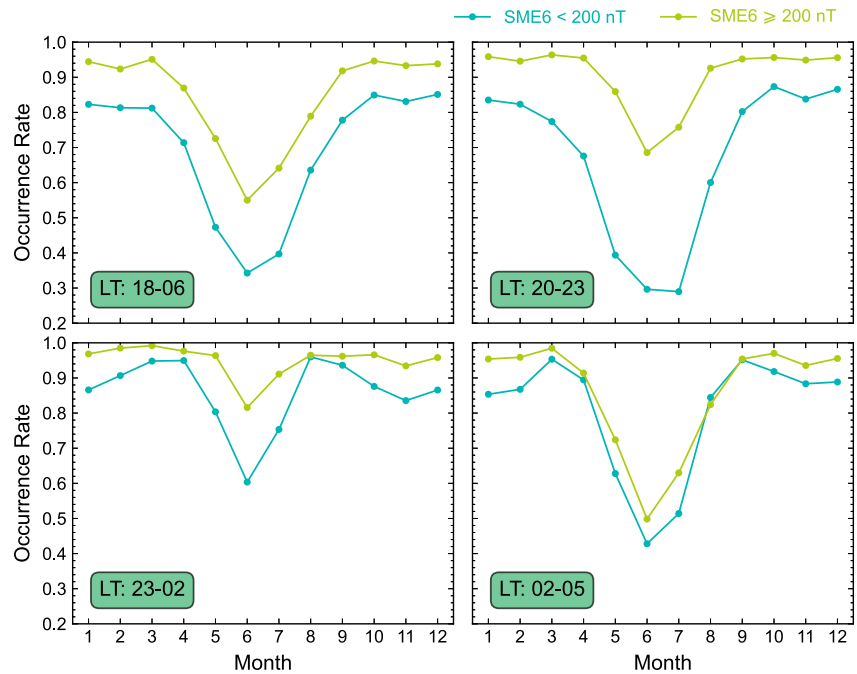

Figure 3. Monthly (seasonal) variations in the occurrence rate of the mid-latitude ionospheric trough across different local times (18–06 LT, i.e., the whole night, and three sub-periods: 20–23 LT, 23–02 LT and 02–05 LT) and two geomagnetic activity levels.

Figure 5 presents the MLIT position distributions for different local hours under different geomagnetic conditions during distinct seasons. An anomaly is noted in the summer at 18 LT, attributed to an exceptionally low occurrence rate of the MLIT at that time, resulting in an insufficient sample size (less than 10). Variations in the MLIT position in relation to LT exhibit slight, season-dependent discrepancies. During the equinoxes, a consistent decrease in the MLAT of MLIT position precedes midnight, reaching a nadir at 00 LT, followed by a phase of relative stability extending from 00 LT to 05 LT, and a marginal increase from 05 LT to 06 LT. Both summer and winter exhibit a similar diurnal pattern to the equinoxes; however, during summer, this steady state interval spans from 03 LT to 05 LT, whereas in winter, it extends from 21 LT to 01 LT, with the amplitude of diurnal variability being the greatest in summer and lowest in winter. Parker et al. (2018) performed a modeling study and observed a similar trend in MLIT's LT variations from September to December in 2002. When contrasting the distributions under different levels of geomagnetic activity, an amplification in the diurnal variability under intense geomagnetic activity becomes evident (on the right of Figure 5), particularly during equinox and summer. Additionally, it is observed that the MLAT of MLIT position decrease during the LT interval from 19 LT to 06 LT under elevated geomagnetic conditions. However, an increase in the MLAT of MLIT position during winter and equinoxes is noted between 18 and 19 LT, suggesting that the physical mechanisms responsible for the MLIT formation on either side of 19 LT may differ.

3.3. Geomagnetic Activity Dependence

Figure 6 presents MLIT position distributions across different SME6 index ranges for 120°W and 90°W longitude bands. It is observable that throughout the nighttime LT sectors, the medians of the MLIT position distributions exhibit a decreasing trend with increasing SME6 index. A decline of approximately 5° in the median values is noted, ranging from $0 \leqslant$ SME6 $<$ 100 nT to SME6 $\geqslant$ 700 nT. Horvath and Essex (2003) used the Kp index to find that the MLIT significantly moves toward the equator at high Kp levels, which they attributed to the expansion of the auroral oval, the poleward neighbor of the MLIT. Upon comparing the variations in the MLIT position distribution across other LT sectors relative to the SME6 index, it is discerned that the changes during the pre-midnight sector are relatively minor. The general trend of the MLATs of MLIT position descending with increasing SME6 index is not as evident before midnight. However, a significant declining trend is observed during the midnight and post-midnight sectors. This highlights the asymmetric impact of geomagnetic activity on

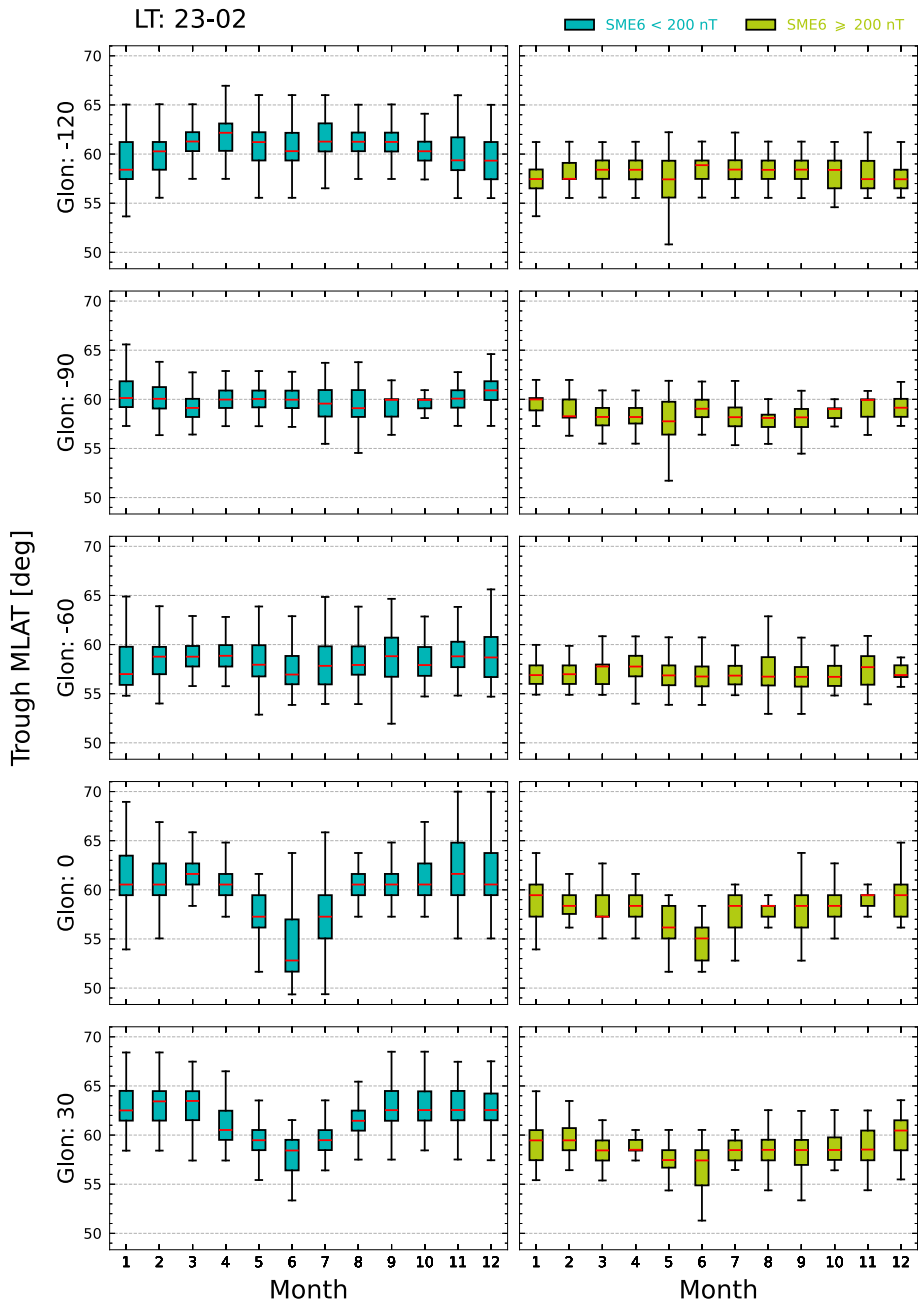

Figure 4. Monthly (seasonal) variations of the mid-latitude ionospheric trough minimum position in midnight (23–02 LT), in different longitude bands (120°W, 90°W, 60°W, 0° and 30°E) and under two different geomagnetic activity levels.

the MLIT position at different local times, suggesting varied mechanisms are at play. The effect intensifies during and after midnight, contrasting with the stronger influence of geomagnetic activity on the MLIT occurrence rate before midnight. Le et al. (2017) found that geomagnetic activity has a greater impact on the MLIT position at post-midnight than at pre-midnight, similar to our findings.

3.4. Multiday Periodic Oscillations

We employed the Continuous Wavelet Transform (CWT) to conduct spectral analysis of the SW velocity and the MLIT position. Figure 7 presents the time-series and CWT power spectra of the SW velocity and the MLIT position (denoted by its MLAT). For the MLIT position, we selected data from the 90°W longitude band

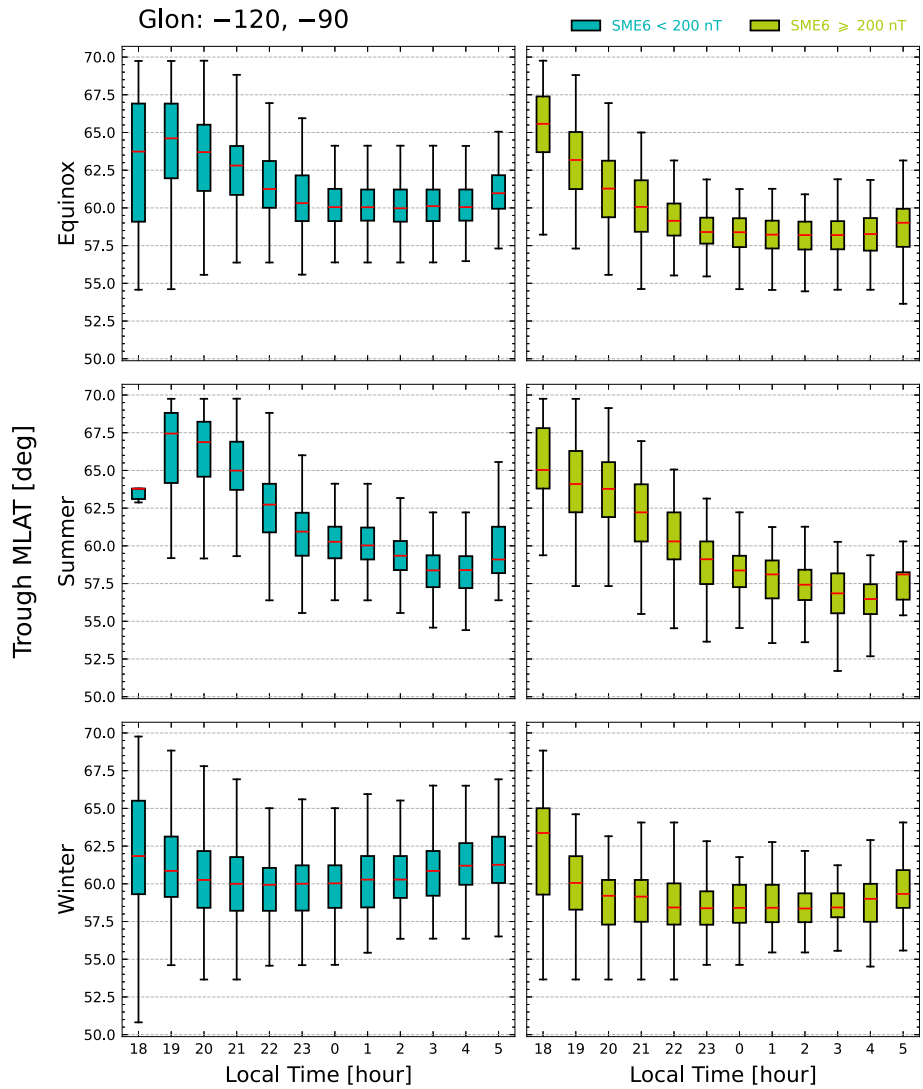

Figure 5. Local time variations of the mid-latitude ionospheric trough minimum position in the 120°W and 90°W longitude bands, in different seasons and under two different geomagnetic activity levels. The three seasons are equinox (March, April, September, and October), summer (May, June, July, and August), and winter (November, December, January, and February).

corresponding to a LT interval of 00–03 LT. Analysis of Figures 7a and 7b reveals that SW velocity fluctuates primarily within the range of 300 km/s to 700 km/s, exhibiting significant variability, whereas the MLIT position oscillates mainly between 57° and 62°, with relatively minor fluctuations. To normalize the time series of SW velocity and the MLIT position, both data sets were first adjusted by subtracting their respective mean and then dividing by their standard deviations. Subsequent application of the CWT yielded power spectra as depicted in Figures 7c and 7d. The power spectra indicate that both SW velocity and the MLIT position exhibit distinct periodic structures, predominantly reflecting a 27-day cycle, followed by 13.5-day and 9-day cycles. These periodicities closely align with the Sun's ∼27-day rotation cycle and its second (13.5-day) and third (9-day) harmonics (M. S. He et al., 2011; Temmer et al., 2007). The 27-day cycle, characterized by the longest duration and peak wavelet power, manifests as six structures in the SW velocity spectrum (Figure 7c), four of which exceed the 90% confidence level (outlined by black solid curves) and last for durations exceeding two months. In the MLIT position spectrum (Figure 7d), five structures of the 27-day periodicity correspond well with those in the SW velocity spectrum, but only one of these surpasses the 90% confidence level, the others displaying relatively lower wavelet power. The 13.5-day cycle persists for shorter periods, about one to 2 months, and is identified by four instances in the SW velocity that exceed the 90% confidence level. Although the 13.5-day cycle is also present in the MLIT position, it exhibits universally lower wavelet power which does not exceed the 90%

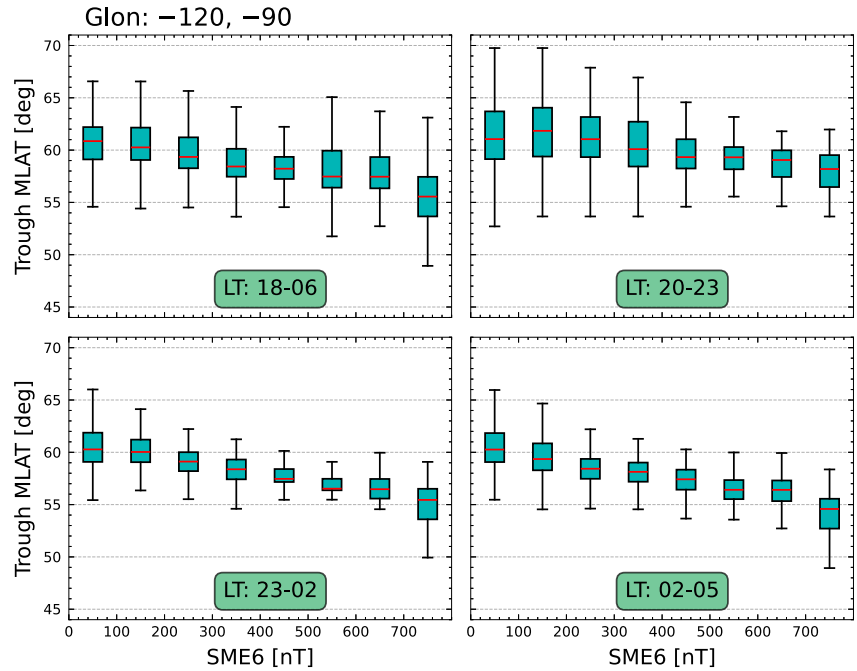

Figure 6. Geomagnetic activity dependence of the mid-latitude ionospheric trough minimum position across different local times (18–06 LT, i.e., the whole night, and three sub-periods: 20–23 LT, 23–02 LT, and 02–05 LT), at the 120°W and 90°W longitude bands. Each subplot contains eight box plots, corresponding to different ranges of the SME6 index: [0 nT, 100 nT), [100 nT, 200 nT), [200 nT, 300 nT), [300 nT, 400 nT), [400 nT, 500 nT), [500 nT, 600 nT), [600 nT, 700 nT), and [700 nT, +∞).

confidence level. The 9-day cycle appears as minor-scale structures with the shortest persistence, generally less than 1 month, and multiple instances exceeding the 90% confidence level are identified in both power spectra. Additionally, the power spectra for both parameters show several smaller-scale structures of less than 9 days, which are more common during the descending and minimum phases of the solar cycle (Gibson et al., 2009; Temmer et al., 2007). These structures have short durations with lower wavelet power and are not discussed further in this article. Overall, there is a notable correspondence between the periodic structures in the power spectra of SW velocity and the MLIT position, though the wavelet power of the latter tends to be generally lower.

To elucidate the significance of the periodic structures in both power spectra, an integration of their respective wavelet power spectra over time was performed, resulting in the global wavelet power spectra shown in Figures 7e and 7f. The global power spectrum of SW velocity exhibits peaks at 27, 13.5, and 9 days, all exceeding the 90% confidence level. The most significant peak corresponds to the 27-day cycle, followed by the 13.5- and 9-day cycles. Although the MLIT position's global power spectrum peaks also occur at these periods, none reach the 90% confidence level. Here, the most distinguishable is the 27-day cycle, with the 13.5- and 9-day cycles showing approximately equal significance.

To further verify the relationship between the MLIT position and SW velocity, we employed the Cross Wavelet Transform (XWT) and Wavelet Coherence (WTC) techniques. These advanced methods enhance the visualization of the interconnection between their periodic structures. The resulting XWT power spectrum is depicted in Figure 8a, with the WTC spectrum portrayed in Figure 8b. In the WTC spectrum, the orientations of phase arrows quantify the phase lag between SW velocity and the MLIT position. Convention dictates that arrows directed downward signify a leading phase for SW velocity, whereas upward arrows denote a leading phase for the MLIT position (Grinsted et al., 2004). Regions of elevated power, enclosed in black on the XWT spectrum, delineate shared periodic structures between the two parameters, aligning with the CWT power spectrum findings. Notably, the 27-day component exhibit fewer occurrences, yet longer durations, contrasting with the more frequent but ephemeral 13.5-day and 9-day cycles. Correlation analyses from the WTC spectrum reveal regions of heightened coherence closely corresponding to the periodic structures identified in the XWT power spectrum. It is particularly noteworthy that in areas of the WTC spectrum where coherence is elevated, the phase arrows

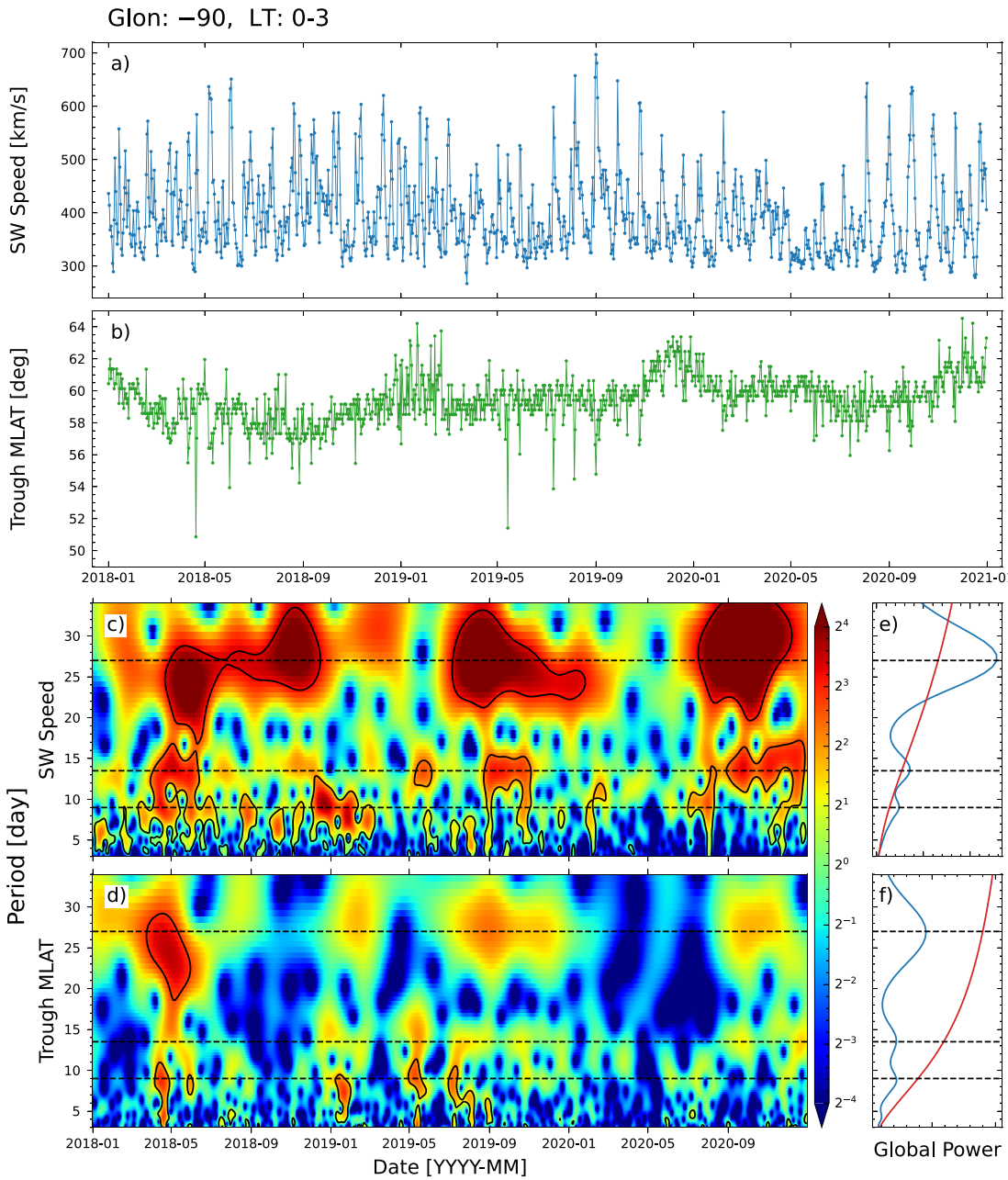

Figure 7. Time-series of solar wind (SW) velocity and the mid-latitude ionospheric trough (MLIT) minimum position at the 90°W longitude band aligned with their Continuous Wavelet Transform (CWT) power spectra. (a)–(b) Time-series of SW velocity and MLIT minimum position's magnetic latitude. (c)–(d) CWT power spectra of the two parameters, with regions exceeding 90% confidence outlined by black solid curves, and 27-day, 13.5-day, 9-day periods are marked with black dashed lines. (e)–(f) Global wavelet power spectra (blue solid lines) of the two parameters, with 27-day, 13.5-day, 9-day periods indicated with black dashed lines and the 90% confidence threshold illustrated by red lines.

predominantly point downward, indicating a leading phase for SW velocity. Such a directional tendency implies statistically a causal relationship between SW velocity and the MLIT position, with SW velocity being the driving factor.

4. Discussion

Karpachev (2003) noted that the MLIT shape varies significantly with longitude, a factor that requires priority consideration. Thus, we first present the longitudinal variation in MLIT position in Figure 2, showing that the

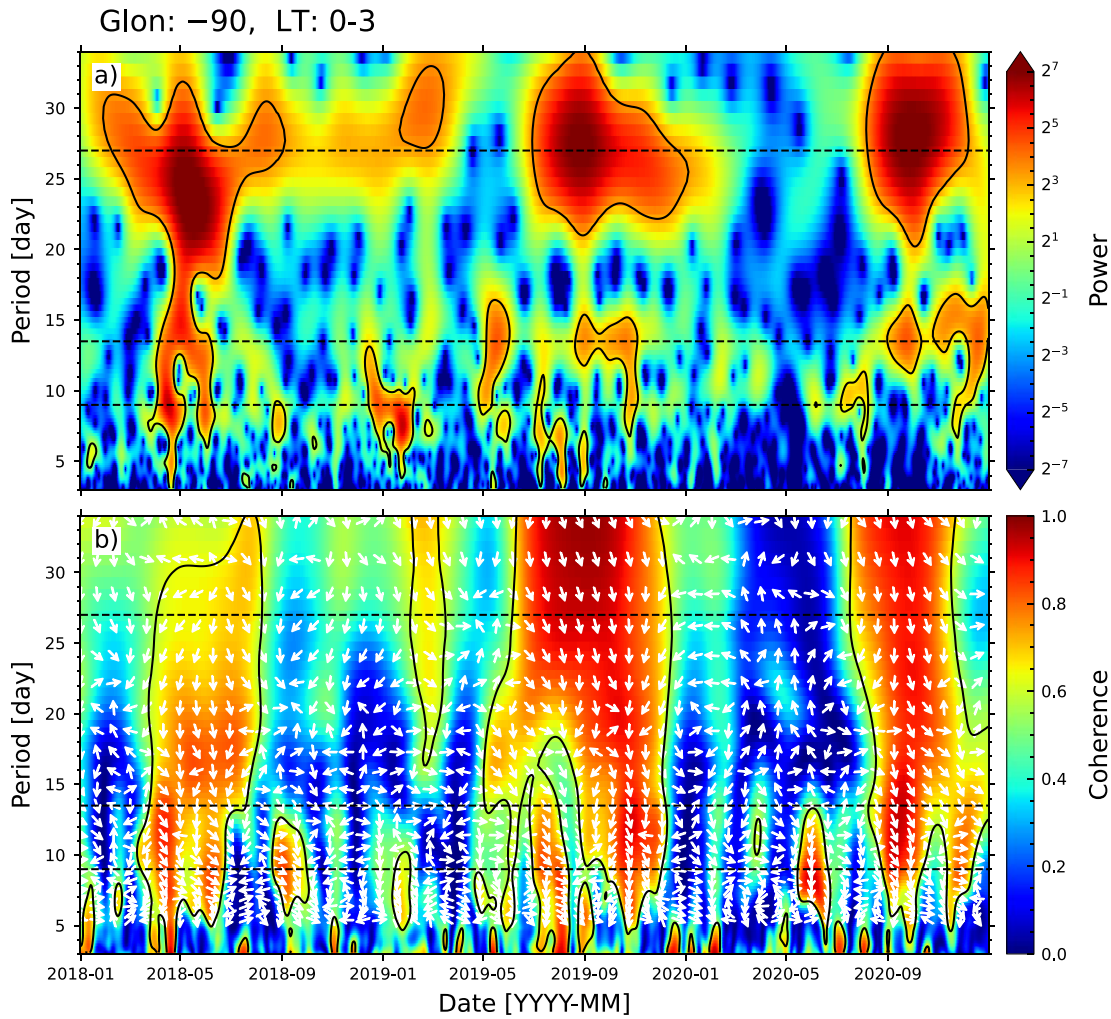

Figure 8. The Cross Wavelet Transform (XWT) power spectrum and Wavelet Coherence (WTC) spectrum of the mid-latitude ionospheric trough (MLIT) minimum position and solar wind (SW) velocity at the 90°W longitude band. (a) XWT power spectrum, where regions exceeding the 95% confidence level are encircled by solid black lines, and 27-day, 13.5-day, 9-day periods are marked with black dashed lines. (b) WTC spectrum, again with regions surpassing the 95% confidence level enclosed by solid black lines. Similarly, black dashed lines indicate 27-day, 13.5-day, and 9-day periods, while white arrows highlight the phase relationship between the MLIT minimum position and the SW velocity.

MLIT is closest to the magnetic equator at 60°W longitude band and furthest at 30°E longitude band. Using 21 years of DMSP satellites data, Yang et al. (2018) reported that the highest MLAT of MLIT position near 19 MLT is observed around 60°W during winter in the Northern Hemisphere. This contradiction may primarily stem from the different effects of neutral winds at various altitudes, considering DMSP satellites are located around 850 km high, whereas our GPS TEC data mainly derives from NmF2 contributions. Due to the importance of the longitudinal variation, we need to restrict the longitude when studying the MLIT's morphological changes and oscillations. Some previous studies investigating the MLIT's oscillations used satellite data and were difficult to consider longitude variations (e.g., M. S. He et al., 2011), while others used global TEC map data without fully considering the longitude constraints (e.g., Castaño et al., 2021; Natali et al., 2020).

Based on the five longitude bands selected in this article, we examined the seasonal variations in the position of MLIT in each longitude band. From Figures 2 and 4, we can conclude that seasonal variations are affected by longitudinal variations, with weak seasonal variations appearing in longitude bands where the MLIT has an equatorward position. However, this relationship is unlikely to be linear. As shown in Figure 2, the MLIT in the 0° longitude band has a more equatorward position than in the 30°E longitude band. However, in Figure 4, the seasonal variations in the 0° longitude band are more noticeable than in the 30°E longitude band.

Karpachev (2003) noted that the MLIT's seasonal variations differ in various longitude sectors. The results of this article may indicate that the position of MLIT varies by longitude, which subsequently leads to different seasonal variations in various longitude sectors.

The recurrent SW speed can directly drive oscillations in the MLIT position (Castaño et al., 2021; M. S. He et al., 2011; Natali et al., 2020). Previous researchers attributed this relation to the effect of SW speed on ionospheric plasma convection. Relative to Earth, the electric field in the high-speed SW can be expressed by the equation $\boldsymbol{E}_{SW} = -\boldsymbol{V}_{SW} \times \boldsymbol{B}_z$ (Burton et al., 1975). Upon the high-speed SW reaching Earth, its enhanced electric field could be mapped along magnetic field lines into ionosphere, directly affecting the local electric field-driven convection of high latitude ionospheric plasma. Consequently, this strengthens the high latitude plasma convection, resulting in the equatorward displacement of the MLIT. To thoroughly examine this process, we utilized SuperDARN radar data to bridge the gap between the SW data and the MLIT.

Figure 9 presents an example of the MLIT position exhibiting a 27-day periodicity at the 90°W longitude band within the time range spanning from 6 August 2019, to 26 October 2019. The time series of several parameters are shown in Figures 9a–9c, which reveals a robust correspondence among the peaks of SW velocity, the nadirs of SW density, the maxima of the SME index and the HMB MLAT, the minima of the MLIT position's MLAT and the CPCP. When the high-speed SW arrived, it strengthened the high latitude ionospheric plasma convection. This was evident from the increase in CPCP and the decrease in HMB MLAT, leading to a lower MLAT of MLIT position. Besides, the high-speed SW were often associated with interplanetary shocks, which could induce geomagnetic storms and substorms (Chao & Lepping, 1974; Zhou & Tsurutani, 2001), as reflected by the substantial increase in SME index. The enhanced geomagnetic activities could expand the equatorward auroral boundary to a lower latitude, resulting in an equatorward shift of the MLIT. To thoroughly analyze the periodic components and their significance, we employed the Lomb-Scargle (LS) periodogram method, as depicted in Figures 9d–9g. Analysis of the LS periodograms reveals that, in this case, the most prominent periodicities in the MLIT position and SW velocity are around 29 days, both exceeding the 90% confidence level. The CPCP has a similar periodicity, whereas the HMB exhibits a 27-day periodicity. Additionally, it is observed that the 13.5-day, 9-day, and more minor-scale periodicities are also present in all the four parameters.

5. Summary and Conclusions

In this study, we used global GPS TEC map data recorded between 1 January 2018, and 31 December 2020, to investigate the morphology changes of nightside MLIT and its position oscillations at specific longitudes. Key findings are summarized as follows:

1. The MLIT position shows discernible longitudinal variation. Generally, the MLAT of MLIT position reaches its minimum at the 60°W longitude band and its maximum at the 30°E longitude band. The differences among the remaining three longitude bands are relatively minor in comparison.
2. The occurrence rate of MLIT exhibits significant seasonal variation, peaking in winter and equinoxes and dipping in summer. And the seasonal variations in the MLIT position show clear differences across longitude bands. Furthermore, intensified geomagnetic activities tend to reduce these seasonal variations.
3. Heightened geomagnetic activities significantly promote the MLIT, especially during the pre-midnight hours in summer and equinoxes, and move it toward the equator, which is pronounced during midnight and post-midnight hours.
4. The MLIT position exhibits clear LT variation, showing a gradual decrease in the MLAT of MLIT position before midnight, stabilization afterward, and a minor resurgence around dawn. Importantly, the LT when this stability occurs varies with the seasons. Moreover, heightened geomagnetic activities tend to amplify the LT variation of the MLIT position.
5. During the solar minimum phase of Solar Cycles 24–25, three distinct periodic components were observed in the MLIT position: 27, 13.5, and 9 days. The 27-day period was the most persistent, followed by the 13.5-day period, while the 9-day period exhibited the shortest duration of the three.
6. The wavelet power spectra reveal the presence of significant periodic structures. These structures correspond to an appreciable increase in the correlation between the MLIT position and SW velocity within the wavelet coherence spectrum. Moreover, the phase relationship suggests that variations in SW velocity typically precede changes in the MLIT position.

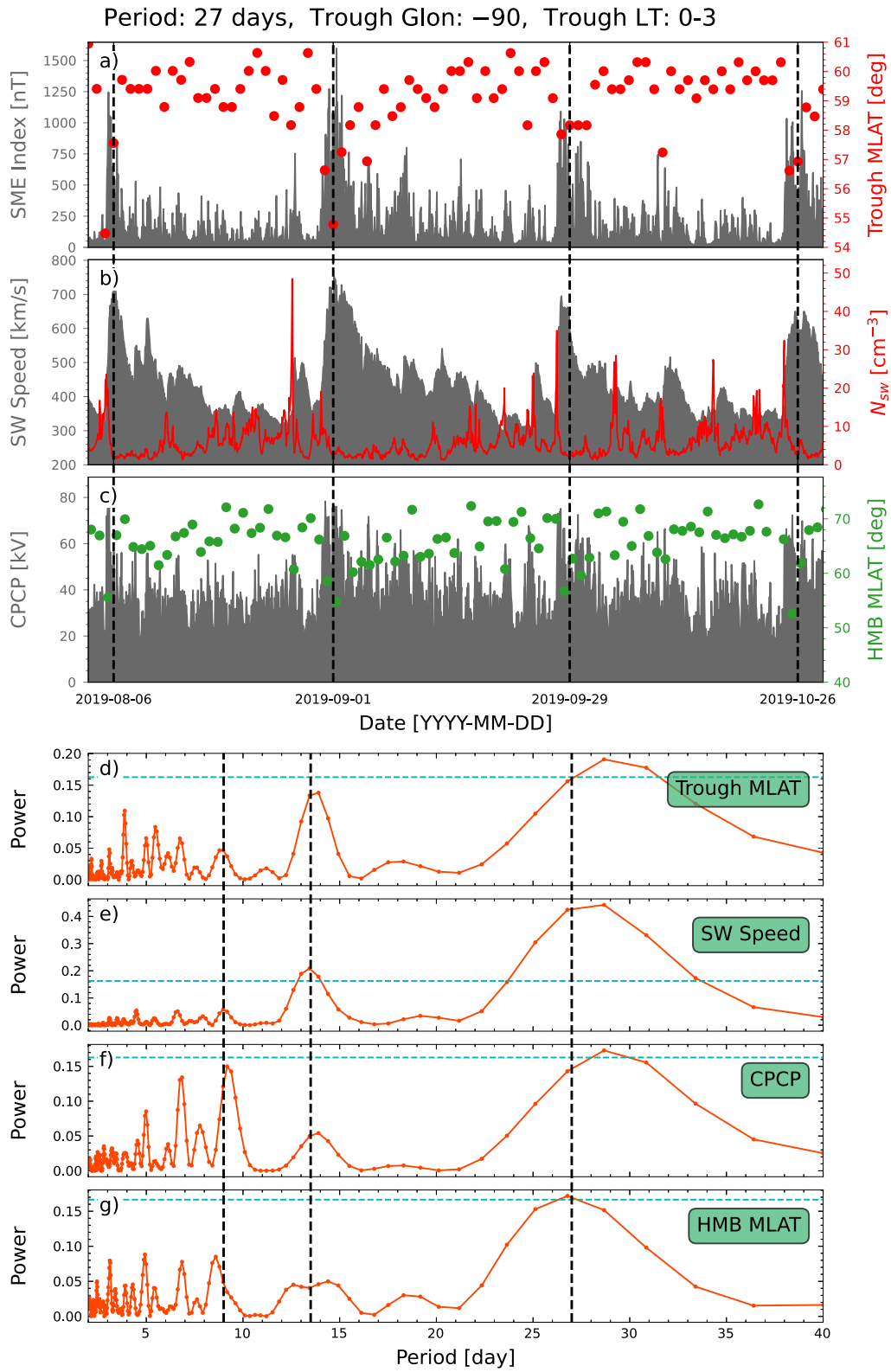

Figure 9. An example of the 27-day periodic oscillation in the mid-latitude ionospheric trough (MLIT) minimum position at the 90°W longitude band. (a) SME index (gray image) and MLIT minimum position's magnetic latitude (red dots). (b) Solar wind (SW) velocity (gray image) and SW density (red solid line). (c) Cross Polar Cap Potential (gray image) and Heppner-Maynard Boundary (blue dots). (d)–(g) The Lomb-Scargle periodograms of these parameters, with the green dashed lines representing the 90% confidence level and the black dashed lines indicating 27-, 13.5-, and 9-day periods.

Data Availability Statement

GPS TEC data products and access through the Madrigal distributed data system are provided to the community (http://www.openmadrigal.org) by the MIT under support from US National Science Foundation grant AGS-1952737. Data for TEC processing is provided from the following organizations: UNAVCO, Scripps Orbit and Permanent Array Center, Institut Geographique National, France, International GNSS Service, The Crustal Dynamics Data Information System, National Geodetic Survey, Instituto Brasileiro de Geografia e Estatística, RAMSAC CORS of Instituto Geográfico Nacional de la República Argentina, Arecibo Observatory, Low-Latitude Ionospheric Sensor Network, Topcon Positioning Systems, Inc., Canadian High Arctic Ionospheric Network, Centro di Ricerche Sismologiche, Système d'Observation du Niveau des Eaux Littorales (SONEL), RENAG: REseau NAtional GPS permanent, GeoNet - the official source of geological hazard information for New Zealand, GNSS Reference Networks, Finnish Meteorological Institute, and SWEPOS—Sweden. The TEC data used in the study are available at Madrigal Database via http://cedar.openmadrigal.org (Anthea Coster & MIT/Haystack Observatory, 2020). The ionospheric convection data were extracted from the SuperDARN convection map data set and are available at Zenodo via https://doi.org/10.5281/zenodo.10875060 (Liu, 2024). The SME index data were downloaded from the SuperMAG website via https://supermag.jhuapl.edu/indices/ (Gjerloev, 2012). The SW and IMF data were obtained from the OMNI data set via https://cdaweb.gsfc.nasa.gov/pub/data/omni/ (Papitashvili & King, 2020a, 2020b).

Acknowledgments
This research is jointly supported by the National Natural Science Foundation of China (No. 42074192) and the Chinese Meridian Project. We gratefully acknowledge the SuperMAG collaborators (https://supermag.jhuapl.edu/info/?page=acknowledgement). We acknowledge the use of SuperDARN data. SuperDARN is a network of radars funded by national scientific funding agencies of Australia, Canada, China, France, Italy, Japan, Norway, South Africa, the United Kingdom, and the United States of America. The authors thank all the data providers.

References

Anthea Coster, & MIT/Haystack Observatory. (2020). Data from the CEDAR Madrigal Database [Dataset]. *CEDAR*. Retrieved from http://cedar.openmadrigal.org/getCitationGroup?id=1016

Bergin, A., Chapman, S. C., & Gjerloev, J. W. (2020). *AE*, D_{ST}, and their SuperMAG counterparts: The effect of improved spatial resolution in geomagnetic indices. *Journal of Geophysical Research: Space Physics*, *125*(5), e2020JA027828. https://doi.org/10.1029/2020JA027828

Burton, R. K., Mcpherron, R. L., & Russell, C. T. (1975). An empirical relationship between interplanetary conditions and *Dst*. *Journal of Geophysical Research*, *80*(31), 4204–4214. https://doi.org/10.1029/JA080i031p04204

Castaño, J. M., Natali, M. P., & Meza, A. (2021). Postmidnight mid-latitude ionospheric trough position oscillations during solar cycle 24. *Advances in Space Research*, *68*(4), 1876–1889. https://doi.org/10.1016/j.asr.2021.04.027

Chao, J., & Lepping, R. (1974). A correlative study of SSC's, interplanetary shocks, and solar activity. *Journal of Geophysical Research*, *79*(13), 1799–1807. https://doi.org/10.1029/JA079i013p01799

Chisham, G., Lester, M., Milan, S., Freeman, M., Bristow, W., Grocott, A., et al. (2007). A decade of the Super Dual Auroral Radar Network (SuperDARN): Scientific achievements, new techniques and future directions. *Surveys in Geophysics*, *28*(1), 33–109. https://doi.org/10.1007/s10712-007-9017-8

Collis, P. N., & Häggström, I. (1988). Plasma convection and auroral precipitation processes associated with the main ionospheric trough at high latitudes. *Journal of Atmospheric and Terrestrial Physics*, *50*(4–5), 389–404. https://doi.org/10.1016/0021-9169(88)90024-4

Emery, B. A., Richardson, I. G., Evans, D. S., & Rich, F. J. (2009). Solar wind structure sources and periodicities of auroral electron power over three solar cycles. *Journal of Atmospheric and Solar-Terrestrial Physics*, *71*(10–11), 1157–1175. https://doi.org/10.1016/j.jastp.2008.08.005

Gibson, S. E., Kozyra, J. U., de Toma, G., Emery, B. A., Onsager, T., & Thompson, B. J. (2009). If the Sun is so quiet, why is the Earth ringing? A comparison of two solar minimum intervals. *Journal of Geophysical Research*, *114*(A9), A09105. https://doi.org/10.1029/2009JA014342

Gjerloev, J. W. (2012). The SuperMAG data processing technique. *Journal of Geophysical Research*, *117*(A9), A09213. https://doi.org/10.1029/2012JA017683

Grinsted, A., Moore, J. C., & Jevrejeva, S. (2004). Application of the cross wavelet transform and wavelet coherence to geophysical time series. *Nonlinear Processes in Geophysics*, *11*(5/6), 561–566. https://doi.org/10.5194/npg-11-561-2004

He, M. S., Liu, L. B., Wan, W. X., & Zhao, B. Q. (2011). A study on the nighttime midlatitude ionospheric trough. *Journal of Geophysical Research*, *116*(A5), A05315. https://doi.org/10.1029/2010JA016252

He, S. C., Zhang, D. H., Hao, Y. Q., & Xiao, Z. (2020). Statistical study on the occurrence of the ionospheric mid-latitude trough and the variation of trough minimum location over Northern Hemisphere. *Chinese Journal of Geophysics*, *63*(1), 31–46. https://doi.org/10.6038/cjg2020M0564

Horvath, I., & Essex, E. A. (2003). The southern-hemisphere mid-latitude day-time and night-time trough at low-sunspot numbers. *Journal of Atmospheric and Solar-Terrestrial Physics*, *65*(8), 917–940. https://doi.org/10.1016/S1364-6826(03)00113-5

Ishida, T., Ogawa, Y., Kadokura, A., Hiraki, Y., & Häggström, I. (2014). Seasonal variation and solar activity dependence of the quiet-time ionospheric trough. *Journal of Geophysical Research: Space Physics*, *119*(8), 6774–6783. https://doi.org/10.1002/2014JA019996

Karpachev, A. T. (2003). The dependence of the main ionospheric trough shape on longitude, altitude, season, local time, and solar and magnetic activity. *Geomagnetism and Aeronomy C/C of Geomagnetizm I Aeronomiia*, *43*(2), 239–251.

Karpachev, A. T., Deminov, M. G., & Afonin, V. V. (1996). Model of the mid-latitude ionospheric trough on the base of Cosmos-900 and Intercosmos-19 satellites data. *Advances in Space Research*, *18*(6), 221–230. https://doi.org/10.1016/0273-1177(95)00928-0

Krankowski, A., Shagimuratov, I. I., Ephishov, I. I., Krypiak-Gregorczyk, A., & Yakimova, G. (2009). The occurrence of the mid-latitude ionospheric trough in GPS-TEC measurements. *Advances in Space Research*, *43*(11), 1721–1731. https://doi.org/10.1016/j.asr.2008.05.014

Krieger, A. S., Timothy, A. F., & Roelof, E. C. (1973). A coronal hole and its identification as the source of a high velocity solar wind stream. *Solar Physics*, *29*(2), 505–525. https://doi.org/10.1007/BF00150828

Le, H. J., Yang, N., Liu, L. B., Chen, Y. D., & Zhang, H. (2017). The latitudinal structure of nighttime ionospheric TEC and its empirical orthogonal functions model over North American sector. *Journal of Geophysical Research: Space Physics*, *122*(1), 963–977. https://doi.org/10.1002/2016JA023361

Lee, I. T., Wang, W. B., Liu, J. Y., Chen, C. Y., & Lin, C. H. (2011). The ionospheric midlatitude trough observed by FORMOSAT-3/COSMIC during solar minimum. *Journal of Geophysical Research*, *116*(A6), A06311. https://doi.org/10.1029/2010JA015544

Liu, X.-L. (2024). The ionospheric convection data extracted from the SuperDARN convection map dataset [Dataset]. *Zenodo*. https://doi.org/10.5281/zenodo.10875060

Matyjasiak, B., Przepiórka, D., & Rothkaehl, H. (2016). Seasonal variations of mid-latitude ionospheric trough structure observed with DEMETER and COSMIC. *Acta Geophysica*, *64*(6), 2734–2747. https://doi.org/10.1515/acgeo-2016-0102

Moffett, R. J., & Quegan, S. (1983). The mid-latitude trough in the electron concentration of the ionospheric F-layer: A review of observations and modelling. *Journal of Atmospheric and Terrestrial Physics*, *45*(5), 315–343. https://doi.org/10.1016/S0021-9169(83)80038-5

Muldrew, D. B. (1965). F-layer ionization troughs deduced from Alouette data. *Journal of Geophysical Research*, *70*(11), 2635–2650. https://doi.org/10.1029/JZ070i011p02635

Natali, M. P., Castaño, J. M., & Meza, A. (2020). The northern and southern mid-latitude ionospheric trough using global IGS vTEC maps. *Advances in Space Research*, *65*(9), 2119–2130. https://doi.org/10.1016/j.asr.2019.09.058

Newell, P. T., & Gjerloev, J. W. (2011). Evaluation of SuperMAG auroral electrojet indices as indicators of substorms and auroral power. *Journal of Geophysical Research*, *116*(A12), A12211. https://doi.org/10.1029/2011JA016779

Nishitani, N., Ruohoniemi, J. M., Lester, M., Baker, J. B. H., Koustov, A. V., Shepherd, S. G., et al. (2019). Review of the accomplishments of mid-latitude Super Dual Auroral Radar Network (SuperDARN) HF radars. *Progress in Earth and Planetary Science*, *6*, 1–57. https://doi.org/10.1186/s40645-019-0270-5

Papitashvili, N. E., & King, J. H. (2020a). OMNI 1-min data [Dataset]. *NASA Space Physics Data Facility*. https://doi.org/10.48322/45bb-8792

Papitashvili, N. E., & King, J. H. (2020b). OMNI hourly data [Dataset]. *NASA Space Physics Data Facility*. https://doi.org/10.48322/1shr-ht18

Parker, J. A. D., Pryse, S. E., Jackson-Booth, N., & Buckland, R. A. (2018). Modelling the main ionospheric trough using the Electron Density Assimilative Model (EDAM) with assimilated GPS TEC. *Annales Geophysicae*, *36*(1), 125–138. https://doi.org/10.5194/angeo-36-125-2018

Prölss, G. W. (2007). The equatorward wall of the subauroral trough in the afternoon/evening sector. *Annales Geophysicae*, *25*(3), 645–659. https://doi.org/10.5194/angeo-25-645-2007

Pryse, S. E., Kersley, L., Malan, D., & Bishop, G. J. (2006). Parameterization of the main ionospheric trough in the European sector. *Radio Science*, *41*(05), 1–9. https://doi.org/10.1029/2005RS003364

Rideout, W., & Coster, A. (2006). Automated GPS processing for global total electron content data. *GPS Solutions*, *10*(3), 219–228. https://doi.org/10.1007/s10291-006-0029-5

Rishbeth, H., Gordon, R., Rees, D., & Fuller-Rowell, T. J. (1985). Modelling of thermospheric composition changes caused by a severe magnetic storm. *Planetary and Space Science*, *33*(11), 1283–1301. https://doi.org/10.1016/0032-0633(85)90007-8

Rodger, A. S. (2008). The mid-latitude trough—Revisited. In *Midlatitude ionospheric dynamics and disturbances* (pp. 25–33). American Geophysical Union (AGU). https://doi.org/10.1029/181GM04

Rodger, A. S., Brace, L. H., Hoegy, W. R., & Winningham, J. D. (1986). The poleward edge of the mid-latitude trough—Its formation, orientation and dynamics. *Journal of Atmospheric and Terrestrial Physics*, *48*, 715–728. https://doi.org/10.1016/0021-9169(86)90021-8

Rodger, A. S., Moffett, R. J., & Quegan, S. (1992). The role of ion drift in the formation of ionisation troughs in the mid-and high-latitude ionosphere—A review. *Journal of Atmospheric and Terrestrial Physics*, *54*(1), 1–30. https://doi.org/10.1016/0021-9169(92)90082-V

Ruohoniemi, J., Greenwald, R., Baker, K., Villain, J.-P., Hanuise, C., & Kelly, J. (1989). Mapping high-latitude plasma convection with coherent HF radars. *Journal of Geophysical Research*, *94*(A10), 13463–13477. https://doi.org/10.1029/JA094iA10p13463

Scali, J. L. (1992). *The mid-latitude trough. a review* (Technical Report). Massachusetts University, Center for Atmospheric Research.

Schunk, R. W., Banks, P. M., & Raitt, W. J. (1976). Effects of electric fields and other processes upon the nighttime high-latitude F layer. *Journal of Geophysical Research*, *81*(19), 3271–3282. https://doi.org/10.1029/JA081i019p03271

Sharp, G. W. (1966). Midlatitude trough in the night ionosphere. *Journal of Geophysical Research*, *71*(5), 1345–1356. https://doi.org/10.1029/JZ071i005p01345

Shepherd, S. (2014). Altitude-adjusted corrected geomagnetic coordinates: Definition and functional approximations. *Journal of Geophysical Research: Space Physics*, *119*(9), 7501–7521. https://doi.org/10.1002/2014JA020264

Spiro, R. W., Heelis, R. A., & Hanson, W. B. (1978). Ion convection and the formation of the mid-latitude F region ionization trough. *Journal of Geophysical Research*, *83*(A9), 4255–4264. https://doi.org/10.1029/JA083iA09p04255

Spiro, R. W., Heelis, R. A., & Hanson, W. B. (1979). Rapid subauroral ion drifts observed by Atmosphere Explorer C. *Geophysical Research Letters*, *6*(8), 657–660. https://doi.org/10.1029/GL006i008p00657

Temmer, M., Vršnak, B., & Veronig, A. M. (2007). Periodic appearance of coronal holes and the related variation of solar wind parameters. *Solar Physics*, *241*(2), 371–383. https://doi.org/10.1007/s11207-007-0336-1

Thomas, E. G., & Shepherd, S. G. (2018). Statistical patterns of ionospheric convection derived from mid-latitude, high-latitude, and polar SuperDARN HF radar observations. *Journal of Geophysical Research: Space Physics*, *123*(4), 3196–3216. https://doi.org/10.1002/2018JA025280

Tulunay, Y. K. (1973). Global electron density distributions from the Ariel 3 satellite at mid-latitudes during quiet magnetic periods. *Journal of Atmospheric and Terrestrial Physics*, *35*(2), 233–254. https://doi.org/10.1016/0021-9169(73)90090-1

Vierinen, J., Coster, A. J., Rideout, W. C., Erickson, P. J., & Norberg, J. (2016). Statistical framework for estimating GNSS bias. *Atmospheric Measurement Techniques*, *9*(3), 1303–1312. https://doi.org/10.5194/amt-9-1303-2016

Voiculescu, M., Nygrén, T., Aikio, A., & Kuula, R. (2010). An olden but golden EISCAT observation of a quiet-time ionospheric trough. *Journal of Geophysical Research*, *115*(A10), A10315. https://doi.org/10.1029/2010JA015557

Voiculescu, M., Virtanen, I., & Nygrén, T. (2006). The F-region trough: Seasonal morphology and relation to interplanetary magnetic field. *Annales Geophysicae*, *24*(1), 173–185. https://doi.org/10.5194/angeo-24-173-2006

Werner, S., & Prölss, G. W. (1997). The position of the ionospheric trough as a function of local time and magnetic activity. *Advances in Space Research*, *20*(9), 1717–1722. https://doi.org/10.1016/S0273-1177(97)00578-4

Whalen, J. A. (1989). The daytime F layer trough and its relation to ionospheric-magnetospheric convection. *Journal of Geophysical Research*, *94*(A12), 17169–17184. https://doi.org/10.1029/JA094iA12p17169

Yang, N., Le, H., Liu, L., & Zhang, R. (2018). Statistical behavior of the longitudinal variations of the evening topside mid-latitude trough position in both northern and southern hemispheres. *Journal of Geophysical Research: Space Physics*, *123*(5), 3983–3997. https://doi.org/10.1029/2017JA025048

Yang, N., Le, H. J., & Liu, L. B. (2015). Statistical analysis of ionospheric mid-latitude trough over the Northern Hemisphere derived from GPS total electron content data. *Earth, Planets and Space*, *67*, 1–11. https://doi.org/10.1186/s40623-015-0365-1

Yizengaw, E., Wei, H., Moldwin, M. B., Galvan, D., Mandrake, L., Mannucci, A., & Pi, X. (2005). The correlation between mid-latitude trough and the plasmapause. *Geophysical Research Letters*, *32*(10), L10102. https://doi.org/10.1029/2005GL022954

Zhou, X., & Tsurutani, B. T. (2001). Interplanetary shock triggering of nightside geomagnetic activity: Substorms, pseudobreakups, and quiescent events. *Journal of Geophysical Research*, *106*(A9), 18957–18967. https://doi.org/10.1029/2000JA003028